

Highly Ligand-Directed and Size-Dependent Photothermal Properties of Magnetite Particles

Haibao Peng, Shiwei Tang, Ye Tian, Rui Zheng, Lei Zhou, and Wuli Yang*

The development of cancer photothermal therapies, many of which rely on photothermal agents, has received significant attention in recent years. In this work, various ligands-stabilized magnetite (Fe_3O_4) particles are fabricated and utilized as a photothermal agents for in vivo tumor-imaging-guided photothermal therapy. Fe_3O_4 particles stabilized by macromolecular ligands as, e.g. polyethylene glycol (PEG), exhibit a superior and more stable photothermal effect compared to Fe_3O_4 particles stabilized by small molecules like citrate, due to their stronger ability of antioxidation. In addition, the photothermal effect of Fe_3O_4 particles is revealed to increase with size, which is attributed to the redshift of Vis-NIR spectra. Fe_3O_4 particles injected intravenously into mice can be accumulated in the tumor by the application of an external magnetic field, as revealed by magnetic resonance imaging. In vivo photothermal therapy test of PEG-stabilized Fe_3O_4 further achieves better tumor ablation effect. Overall, this study demonstrates efficient imaging-guided photothermal therapy of cancer that is based on Fe_3O_4 particles of optimized size and with optimized ligands. It is expected that the ligand-directed and size-dependent photothermal effect will provide more approaches in the design of novel materials.

1. Introduction

The development of nanoparticles has been intensively pursued for their fundamental scientific significance and broad technological applications.^[1] Various kinds of nanoparticles have been extensively investigated for their unique electrical, magnetic, and optical properties, such as semiconductors, magnetic materials, and metallic particles.^[2] In particular, magnetite nanoparticles (Fe_3O_4 NPs) have recently attracted considerable

researchers' interest owing to their unique magnetic features and ideal candidates for their applications in biomedicine,^[3] bioseparation,^[4] sensors,^[5] and therapeutics.^[6] Therefore, great efforts have been devoted to fabrication of water-dispersible Fe_3O_4 NPs with controllable sizes, desirable surface properties, and fast magnetic response.^[7] As we all know, the ligands in the synthesis process are of key importance and give rise to significant surface effects on the physicochemical properties of the nanoparticles.^[8] For example, the role of surface ligands has been explored the effect of magnetic resonance (MR) applications and magnetic resonance relaxivity,^[9] and hydrophobic nanoparticles can be transformed into water-dispersible nanoparticles by exchanging the hydrophobic ligands with hydrophilic ligands.^[10] Additionally, the size of the particles is also very important accounting for their biological and physicochemical properties, such as cellular uptake, bio-distribution,

and other fundamental magnetic properties.^[10a] It should be noted that Fe_3O_4 particles exhibit unique size-dependent and remarkably enhanced molar extinction coefficients in the NIR region.^[11] Therefore, the ligand and size of magnetic nanoparticles are important not only for understanding the behavior of existing materials but also for developing novel nanomaterials with superior properties.

Photothermal therapy (PTT) has drawn clinical interests and much attention due to its minimal invasiveness and highly specific selectivity to targeting sites in cancer treatment.^[12] In recent years, large quantities of near infrared (NIR) absorbing nanomaterials such as gold nanoparticles,^[13] carbon nanomaterials,^[14] transition metal sulfide or oxide nanoparticles^[15] and other organic polymers (e.g., polydopamine and polypyrrole)^[16] have been widely explored as photothermal agents. Very recently, the photothermal effect of magnetic nanoparticles has been reported, which could be used as a good PTT agent.^[17] However, to the best of our knowledge, the impacts of ligands or sizes on the photothermal properties of magnetic nanoparticle has been rarely reported to date, which is very important to the development of nanotechnology.^[18] Hence, there is still much room to improve photothermal effects and stability of magnetic nanoparticles induced by the ligands and sizes to realize imaging-guided cancer therapy.

In this work, the Fe_3O_4 magnetic particles were developed with various ligands and sizes as PTT agents. Tumor targeting

H. B. Peng, Y. Tian, R. Zheng, Prof. W. L. Yang
 State Key Laboratory of Molecular Engineering of Polymers and Department of Macromolecular Science
 Fudan University
 Shanghai 200433, China
 E-mail: wlyang@fudan.edu.cn

Dr. S. W. Tang
 Department of Physics
 Ningbo University
 Zhejiang 315211, China

Prof. L. Zhou
 State Key Laboratory of Surface Physics
 Key Laboratory of Micro and Nano Photonic Structures (Ministry of Education) and Collaborative Innovation Center of Advanced Microstructures
 Fudan University
 Shanghai 200433, China

DOI: 10.1002/ppsc.201600071



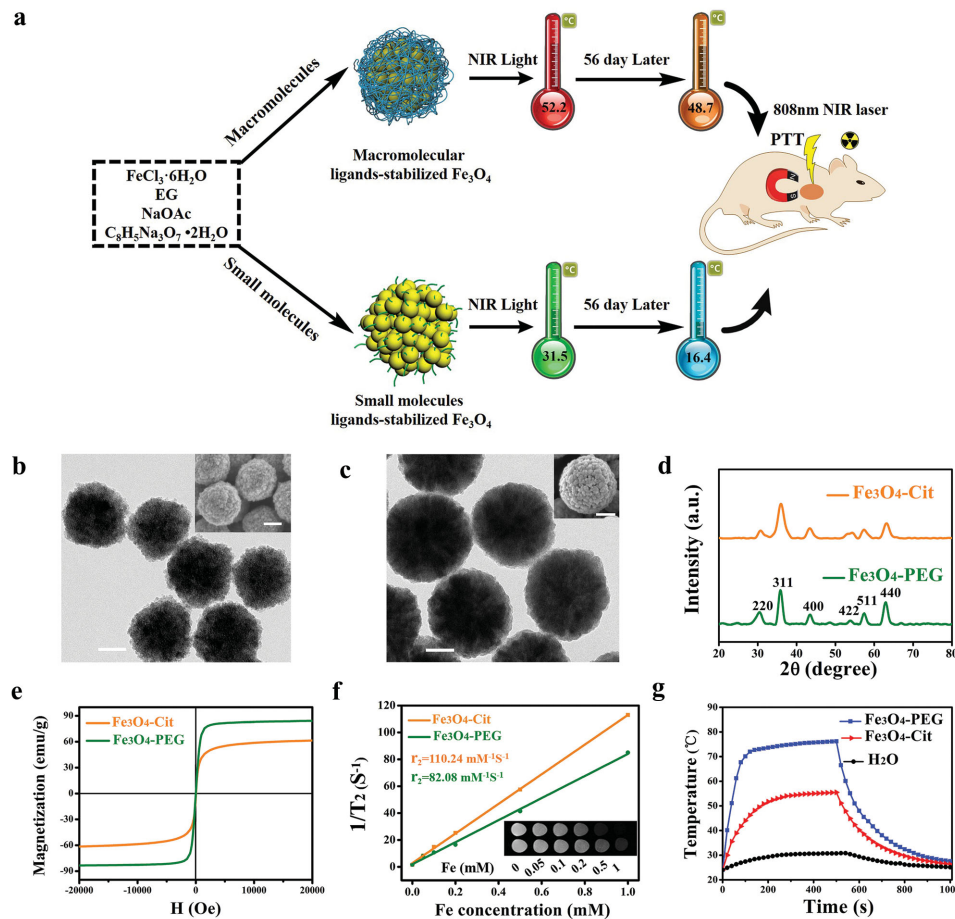


Figure 1. Preparation and characterization of Fe_3O_4 particles. a) Schematic illustration to show the synthesis of Fe_3O_4 particles, the subsequent photothermal properties, and the MR imaging-guided photothermal therapy. b,c) TEM images of b) $\text{Fe}_3\text{O}_4\text{-Cit}$ (240 nm) and c) $\text{Fe}_3\text{O}_4\text{-PEG}$ (300 nm), the insets are the FESEM images. The bar is 100 nm. d) The XRD patterns of $\text{Fe}_3\text{O}_4\text{-Cit}$ and $\text{Fe}_3\text{O}_4\text{-PEG}$ particles. e) Magnetization loops of $\text{Fe}_3\text{O}_4\text{-Cit}$ and $\text{Fe}_3\text{O}_4\text{-PEG}$ particles. f) T_2 relaxation rates ($1/T_2 (\text{s}^{-1})$) as a function of iron concentration (mM) of Fe_3O_4 particles in aqueous medium. Inset: T_2 -weighted MR images of Fe_3O_4 particles (upper: $\text{Fe}_3\text{O}_4\text{-Cit}$; lower: $\text{Fe}_3\text{O}_4\text{-PEG}$) dispersions with different concentrations. g) The photothermal effects of $\text{Fe}_3\text{O}_4\text{-Cit}$ (240 nm) and $\text{Fe}_3\text{O}_4\text{-PEG}$ (300 nm) aqueous dispersions at the concentration of 50 $\mu\text{g mL}^{-1}$ were measured by laser irradiation ($\lambda = 808 \text{ nm}, 6.6 \text{ W cm}^{-2}$). H_2O is used as a negative control.

with magnetic particles induced by an applied external magnetic field (MF) relies on physical forces to enhance tumor accumulation of therapeutic agents. Compared to small molecular ligands, the macromolecular ligands-stabilized Fe_3O_4 particles exhibited more excellent and stable photothermal effect, which could provide a potential clinical application of cancer therapies. Full wave numerical simulations of Fe_3O_4 particles with different sizes also indicated the same conclusion. Our latest work further deliberately demonstrated that Fe_3O_4 magnetic particles could also be used as a good photothermal agent by modulated ligands or particles sizes (Figure 1a). We expect that these excellent and stable photothermal agents based on ligands and sizes may be a promising approach for further exploration photothermal agents.

2. Results and Discussion

The magnetite particles were synthesized using a solvothermal method according to the literature protocol with slight

modifications.^[19] As we know, citric acid is the classic ligand of the preparation Fe_3O_4 particles, and biocompatible citric acid is used as an electrostatic stabilizer and also plays a vital role in the charge density on the surface.^[20] The detailed morphological and structural features of citrate-stabilized Fe_3O_4 particles ($\text{Fe}_3\text{O}_4\text{-Cit}$) and polyethylene glycol-stabilized Fe_3O_4 particles ($\text{Fe}_3\text{O}_4\text{-PEG}$) were examined by transmission electron microscope (TEM) and field-emission scanning electron microscope (FESEM) (Figure 1b,c). The obtained citrate-stabilized Fe_3O_4 and PEG-stabilized Fe_3O_4 particles were well-dispersed in water and showed relatively uniform sizes with an average diameter of 240 ± 15 and 300 ± 10 nm, respectively. Wide-angle X-ray diffraction (XRD) pattern demonstrated that all the diffraction peaks of $\text{Fe}_3\text{O}_4\text{-Cit}$ and $\text{Fe}_3\text{O}_4\text{-PEG}$ could be directly indexed to a cubic phase of magnetite (JCPDS 75–1609) (Figure 1d). The magnetic hysteresis loop showed no evident remanence and coercivity, suggesting superparamagnetic nature of these Fe_3O_4 particles (Figure 1e).^[21] In addition, T_2 -weighted MR images of a series of concentrations of Fe_3O_4 particles dispersions acquired by a 7.0 T MR scanner exhibited increasingly

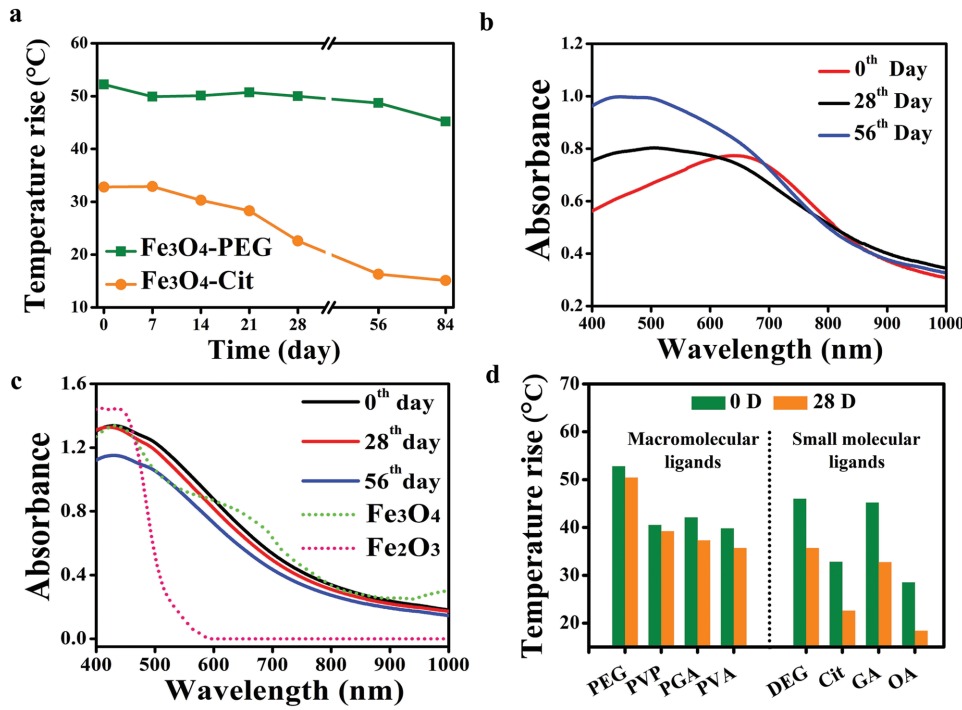


Figure 2. The ligand-directed photothermal properties of Fe₃O₄ particles. a) The change in photothermal effect of Fe₃O₄ particles as a function of storage time. b) The Vis-NIR absorbance spectra of Fe₃O₄-PEG aqueous dispersions at the concentration of 50 µg mL⁻¹ as a function of storage time. c) The Vis-NIR absorbance spectra (solid line) of Fe₃O₄-Cit (50 µg mL⁻¹) for different time points and the simulation curves (dotted line) of Fe₃O₄ and Fe₂O₃ Vis-NIR absorbance. d) Photothermal heating histogram of Fe₃O₄ particles with various macromolecular and various small molecular ligands at 0th day and 28th day. An equivalent concentrations of 50 µg mL⁻¹ Fe₃O₄ particles under exposure to an 808 nm laser for 5 min at a power density of 6.6 W cm⁻².

darker contrast with an increased Fe concentration (Figure 1f). The transverse relaxivity (r_2) values of Fe₃O₄-Cit and Fe₃O₄-PEG were calculated to be 110.24 and 82.08 mM⁻¹ s⁻¹, respectively.

As seen from Figure 1g, the temperatures of fresh Fe₃O₄-PEG and Fe₃O₄-Cit particles at a concentration of 50 µg mL⁻¹ with NIR laser irradiation ($\lambda = 808$ nm, 6.6 W cm⁻²) for 300 s were increased by 52.2 and 31.5 °C, respectively, indicating that the photothermal effect of fresh Fe₃O₄-PEG particles was much better than that of fresh Fe₃O₄-Cit. In addition, according to the previous method,^[22] the photothermal conversion efficiency (η) of Fe₃O₄-PEG and Fe₃O₄-Cit were calculated to be 16.9% and 15.9%, lower than that of polydopamine,^[23] Cu_{2-x}Se,^[24] and iron@iron oxide nanoparticles^[22d] (Tables S1 and S2, Supporting Information). The NIR absorption of Fe₃O₄ particles was higher than that of iron@iron oxide nanoparticles, which was also a key parameter that determined the efficacy of a photothermal conversion agent. Thus, our Fe₃O₄ particles have excellent photothermal effect.

During the experiment, we found the photothermal effect of both Fe₃O₄-PEG and Fe₃O₄-Cit particles decreased with increasing storage time. After 56 d, the temperature change of Fe₃O₄-PEG showed slight decrease to about 48.7 °C (Figure 2a), whereas the temperature change of Fe₃O₄-Cit significantly decreased to about 16.4 °C, revealing Fe₃O₄-PEG particles presented more stable photothermal effect than Fe₃O₄-Cit particles. Considering the photothermal effect change, we then carefully investigated the NIR optical absorbance properties of

Fe₃O₄ particles, as the absorbance intensity in the NIR region is one of the key factors that determine the photothermal capability of a PTT agent.^[25] Interestingly, the Vis-NIR absorbance at 808 nm in the Fe₃O₄-Cit group slowly decreased within 56 d, while the Fe₃O₄-PEG group nearly had no change (Figure 2b). We thought this might be attributed to magnetite (Fe₃O₄) oxidized to maghemite (Fe₂O₃).^[26] To confirm this hypothesis, full wave numerical simulations (COMSOL Multi-physics 3.5, developed by COMSOL, network license) were performed to calculate the absorption of Fe₃O₄-Cit and Fe₂O₃ particles, and the optical constants of Fe₃O₄ and Fe₂O₃ were given by ref.^[27] The simulation results showed that Fe₃O₄ particles had a strong absorption at 808 nm while Fe₂O₃ particles had no NIR absorption at 808 nm (Figure 2c), demonstrating the photothermal effect of Fe₃O₄ particles decreased due to the process of magnetite (Fe₃O₄) oxidized to maghemite (Fe₂O₃).^[28]

To further investigate the process of oxidation, the Fe₃O₄ particles were observed using X-ray photoelectron spectroscopy (XPS). The Fe 3p peaks of Fe₃O₄ were deconvoluted into the Fe (II) and Fe (III) peak.^[29] The peak position and mean relative areas of each constituent peak assigned to Fe (II) and Fe (III) were calculated, these values and standard deviations were listed in Table 1. Since stoichiometric Fe₃O₄ can also be expressed to FeO•Fe₂O₃, the Fe²⁺:Fe³⁺ ratio should be 0.33:0.67. The Fe²⁺:Fe³⁺ = 0.335:0.665 was obtained by Fe₃O₄-PEG (which was preserved for 0 d), and after preserved for 84 d, the ratio of Fe²⁺ and Fe³⁺ turned to 0.333:0.667. In contrast, the Fe²⁺:Fe³⁺

Table 1. Peak positions and FWHM of the XPS Fe 3p peak for Fe^{3+} and Fe^{2+} obtained from Fe_3O_4 particles. The table also shows the ratios of Fe^{2+} and Fe^{3+} in Fe_3O_4 particles using the peak positions and FWHMs obtained from Fe_3O_4 , respectively.

Samples	Fe^{3+} peak position [eV]	Fe^{2+} peak position [eV]	$\text{Fe}^{2+}:\text{Fe}^{3+}$ atomic ratio
	Fe 3p FWHM	Fe 3p FWHM	
$\text{Fe}_3\text{O}_4\text{-Cit}$ (0th day)	55.6 3.1	53.0 3.1	0.316 : 0.684
$\text{Fe}_3\text{O}_4\text{-Cit}$ (84th day)	55.6 3.1	53.0 3.1	0.222 : 0.778
$\text{Fe}_3\text{O}_4\text{-PEG}$ (0th day)	55.6 3.1	53.8 3.1	0.335 : 0.665
$\text{Fe}_3\text{O}_4\text{-PEG}$ (84th day)	55.6 3.1	53.8 3.1	0.333 : 0.667

= 0.316:0.684 was obtained by $\text{Fe}_3\text{O}_4\text{-Cit}$ (which preserved for 0 d), and after preserved for 84 d, the ratio of Fe^{2+} and Fe^{3+} turned to 0.222: 0.778. These results revealed that the Fe^{2+} in $\text{Fe}_3\text{O}_4\text{-Cit}$ was partly oxidized into Fe^{3+} with storage time, while the percentage of Fe^{2+} in $\text{Fe}_3\text{O}_4\text{-PEG}$ had little variation (Figure S1, Supporting Information).^[30] In other words, PEG possessed

stronger protective capability with Fe^{2+} ions and better antioxidation ability in contrast to citrate molecule. It was concluded that the photothermal effect of $\text{Fe}_3\text{O}_4\text{-PEG}$ was much stronger and more stable than that of $\text{Fe}_3\text{O}_4\text{-Cit}$ with time going on.

Likewise, a similar result was also observed when PEG was replaced with other macromolecules, like polyvinyl pyrrolidone (PVP), polyvinyl alcohol (PVA) and polyglutamic acid (PGA), which was attributed to their excellent ability of antioxidation (Figure 2d). However, the photothermal effect of other small molecules, such as oxalic acid (OA), glutamic acid (GA), and diethylene glycol (DEG) stabilized Fe_3O_4 had poor stability owing to their weak ability of antioxidation similar to citrate.

Additionally, the size of $\text{Fe}_3\text{O}_4\text{-Cit}$ and $\text{Fe}_3\text{O}_4\text{-PEG}$ particles could be tuned from 120 to 380 nm by varying the molar quantities of ligands or ferric trichloride (Table S3, Supporting Information). Interestingly, the temperature change was raised with an increasing particle size, indicating that the photothermal effect of these particles had a size-dependent behavior (Figure 3a).^[18b] The larger ones showed an enhanced NIR absorbance owing to the redshift of their Vis-NIR spectra,

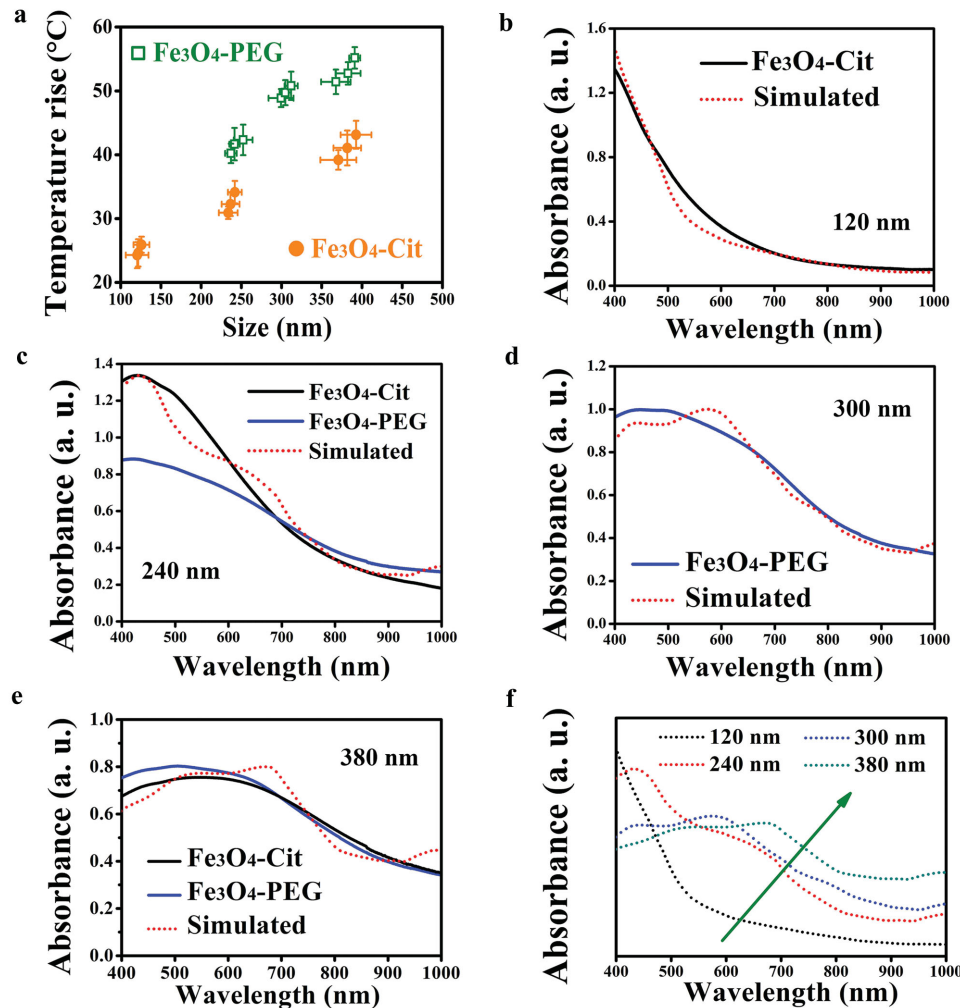


Figure 3. The size-dependent photothermal properties of Fe_3O_4 particles. a) The photothermal properties of size-tuned Fe_3O_4 particles with PEG and citrate ligands. b–e) The Vis-NIR absorbance spectra of a series of $\text{Fe}_3\text{O}_4\text{-Cit}$ and $\text{Fe}_3\text{O}_4\text{-PEG}$ with different sizes from 120 to 380 nm. f) The Vis-NIR absorbance simulation spectra of Fe_3O_4 particles with different diameters from 120 to 380 nm.

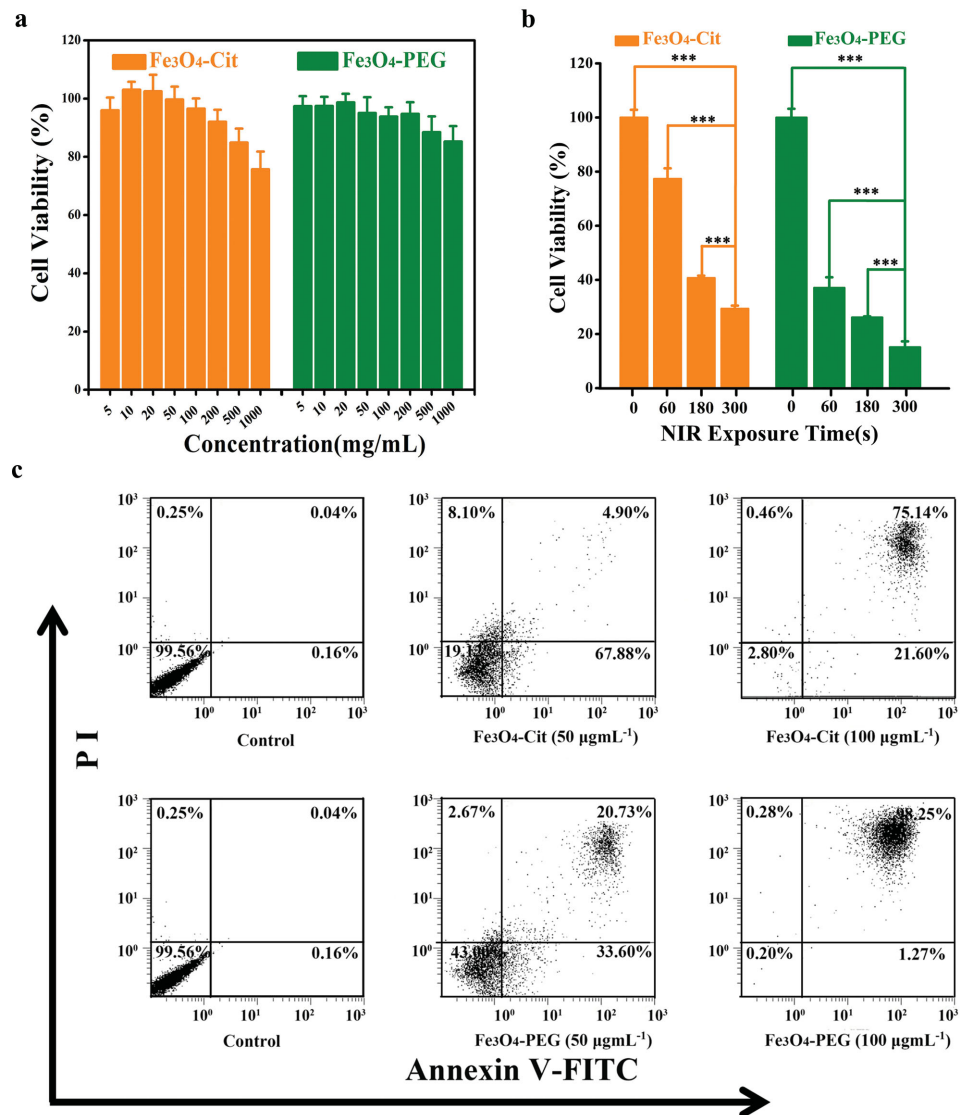


Figure 4. In vitro cell culture experiment. a) Relative viabilities of 293T cells treated with Fe₃O₄-Cit and Fe₃O₄-PEG at different concentrations. b) Relative viabilities of A549 cells treated with Fe₃O₄-Cit and Fe₃O₄-PEG at the concentration of 100 µg mL⁻¹ with NIR laser irradiation ($\lambda = 808$ nm, 6.6 W cm^{-2}) for 0, 60, 180, and 300 s. c) Flow cytometry graphs of A549 cells treated by Fe₃O₄-Cit and Fe₃O₄-PEG at the concentrations of 50 and 100 µg mL⁻¹ with NIR laser irradiation ($\lambda = 808$ nm, 6.6 W cm^{-2}) for 300 s. The treated A549 cells were double stained by Annexin-V-FITC/PI and analyzed by flow cytometry. ***p < 0.001.

which gave rise to an enhanced photothermal effect. Full wave numerical simulations also demonstrated the size-dependent behavior of NIR absorbance (Figure 3b–f).

The bio-compatibility and safety of particles are one of the main concerns in the area of nanomedicine. As Fe₃O₄ particles could gradually decomposed into iron ions and have already been used for clinical MR diagnosis for many years, they have been proven to be biocompatible after administration.^[31] As for Fe₃O₄ particles designed in this work, the cytotoxicity of normal cells (HEK 293T) was first determined by the standard 3-(4,5-dimethyl-2-thiazolyl)-2,5-diphenyltetrazolium bromide (MTT) assay. The results indicated no obvious cytotoxicity even when the nanoparticles concentration was increased to 1000 mg mL⁻¹ (Figure 4a). Next, we studied in vitro photothermal behaviors

in cell culture experiments, and A549 cells were used as a cell model. The photothermal behavior was also estimated using the MTT assay. The A549 cells were incubated with Fe₃O₄-Cit and Fe₃O₄-PEG for 30 min and then irradiated by the 808 nm laser (6.6 W cm^{-2}). About 62.9%, 73.9%, and 84.9% of cells were killed by Fe₃O₄-PEG at the concentration of 100 µg mL⁻¹ for different illumination time of 60, 180, and 300 s, respectively (Figure 4b), and only 22.7%, 59.6%, and 70.6% of cells were killed by Fe₃O₄-Cit particles. Compared with Fe₃O₄-Cit particles, Fe₃O₄-PEG particles with the equivalent doses showed significantly enhanced cancer cell killing ability against the growth of A549 cells.

To clarify the cell death mode after photothermal treatment, cell apoptosis test was conducted by flow cytometry. Figure 4c

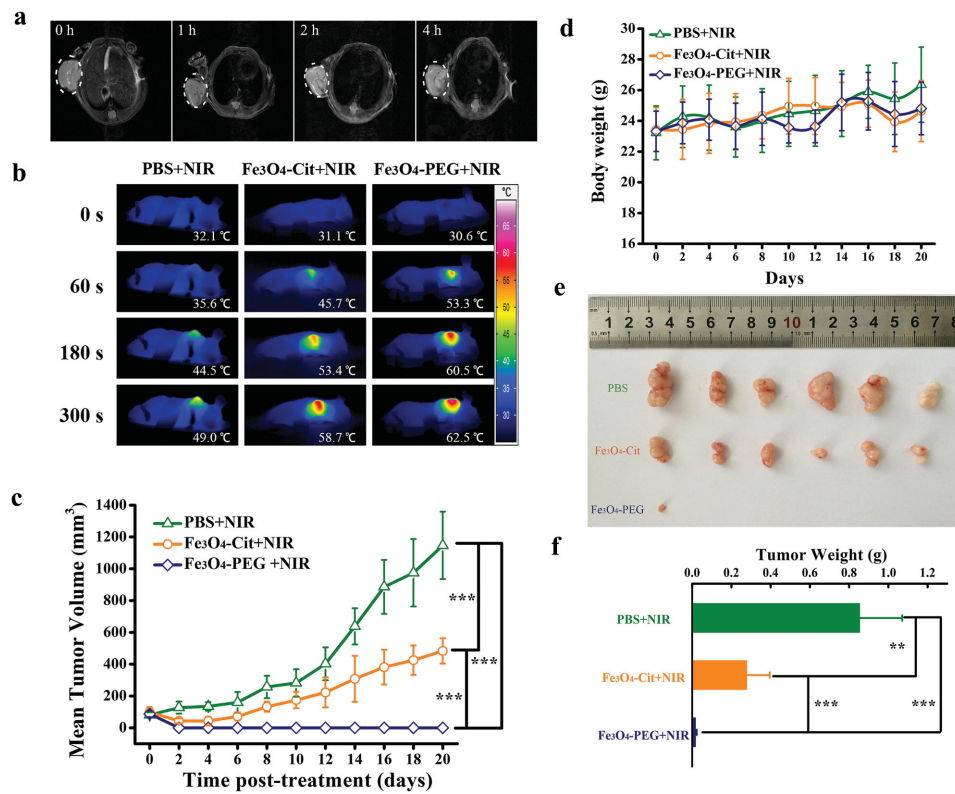


Figure 5. In vivo photothermal therapy. a) In vivo multimodal imaging. T₂-weighted MR images of A549 tumor-bearing mice injected with Fe₃O₄-PEG (0.25 mg mL⁻¹, 200 μL) taken at different time post injection. White circles highlight the tumor site. b) Infrared thermal images of Fe₃O₄-Cit and Fe₃O₄-PEG with the dose of 50 μg under NIR laser irradiation ($\lambda = 808$ nm, 6.6 W cm⁻²) for 0–300 s. c) Tumor growth curves of different groups after treatment. Tumor sizes were measured every 2 d. Means and standard errors are shown. d) Body weight changes were recorded every 2 d after therapy. Means and standard errors are shown. The groups of PBS, Fe₃O₄-Cit and Fe₃O₄-PEG with NIR irradiation for 300 s were statistically identical. e) Photograph of tumors after excision from the groups of PBS, Fe₃O₄-Cit and Fe₃O₄-PEG under NIR irradiation. f) Tumor weights of PBS, Fe₃O₄-Cit and Fe₃O₄-PEG group. **p < 0.01, ***p < 0.001.

exhibited the flow cytometry graphs of the cells by Fe₃O₄-Cit and Fe₃O₄-PEG particles with laser irradiation. Almost no apoptosis or necrosis cells were observed in the group of no NIR treatment. After laser irradiation, the apoptosis rate of cells of Fe₃O₄-PEG (50 μg mL⁻¹) reached 72.8%, while that of Fe₃O₄-Cit (50 μg mL⁻¹) was only 54.3%. The flow cytometry data revealed that cells treated by Fe₃O₄ particles displayed irreversible damage upon photothermal treatment, and their cellular membranes were broken to such an extent that the cells could no longer function nor recover from the damage. Therefore, the mechanism of in vitro PTT was primarily triggered by cell apoptosis.^[32] After that, Calcein Acetoxymethyl ester (Calcein-AM)/Ethidium homodimer-1 (EthD-1) co-staining was carried out to differentiate live and dead cells under confocal fluorescence imaging. Cells exhibited significantly higher EthD-1 signal in Fe₃O₄-PEG treated group than that in Fe₃O₄-Cit treated group (Figure S2, Supporting Information).

Moreover, Fe₃O₄-Cit and Fe₃O₄-PEG particles could be used as MRI probes. We then wondered whether the external magnetic field would guide the tumor specific homing of Fe₃O₄ particles. To enable magnetic targeting, a magnet was securely attached onto the tumor of each mouse by a bandage all the time except being shortly taken off during imaging. Those mice were then imaged by a 7.0 T clinical MR scanner at various

time intervals post injection (Figure 5a).^[33] The MR images of magnetic-targeted tumors showed dramatic darkening effect at the time point of 1 h postinjection, suggesting the high tumor accumulation of Fe₃O₄ particles and imaging-guided targeting PTT to cancer.

Based on the excellent efficacy achieved of in vitro experiments and imaging-guided tests, we further evaluated the in vivo antitumor activity of Fe₃O₄ particles. When the tumor reached ~5 mm in its longest dimension, Fe₃O₄ particles (0.2 mL, 0.25 mg mL⁻¹) were i.v. injected to the A549-bearing mice, and the tumors are attached to magnets. Laser irradiation was performed with an 808 nm NIR laser (6.6 W cm⁻²; spot size, 6 mm × 7 mm) for 300 s at 1 h postinjection. Thermal imaging with an infrared camera thermographic system is used to monitor the efficacy of the treatment (Figure 5b). In contrast, the temperature rise of tumor surface for Group I with injection of PBS was much less significant (only to 49.0 °C after 300 s of laser illumination), showing that NIR laser at such a power density could not induce sufficient heating by itself. For Fe₃O₄-PEG (Group III), the tumor temperature increased rapidly to 62.5 °C within 300 s, which is higher than the temperature from Fe₃O₄-Cit (Group II). During the photothermal treatment, the mice body weights of each group had no obvious change (Figure 5d). At 20th day, mice were euthanized, and

then tumors were excised and weighted (Figure 5e,f). The average weights of tumors for Group I, II, and III were 0.8664 ± 0.2207 g, 0.2820 ± 0.1193 g, and 0.0170 ± 0.0069 g, respectively. Remarkably, the antitumor effect (mean tumor volume) of Group III was particularly prominent and was superior to all the other groups ($p < 0.001$). The statistically significant difference was observed in Group III compared with Group II (Figure 5c). Therefore, the highly biocompatible Fe_3O_4 -PEG showed excellent enhanced photothermal effect compared with Fe_3O_4 -Cit at an equivalent concentration.

3. Conclusion

In summary, we investigated the Fe_3O_4 particles with various ligands as theranostic agents for MR imaging-guided photothermal therapy. Compared with small molecules-stabilized Fe_3O_4 particles, macromolecular ligands-stabilized Fe_3O_4 particles showed more excellent and stable photothermal effect, as macromolecules had stronger ability of protecting the Fe_3O_4 particles from being oxidized. The photothermal property of Fe_3O_4 particles also exhibited size-dependent behavior, and the increasing particle size of Fe_3O_4 particles led to an increase of the photothermal effect. Our research encouraged further explorations of PTT agents based on ligands and sizes for applications in cancer therapy.

4. Experimental Section

Materials: Iron(III) chloride ($\text{FeCl}_3 \cdot 6\text{H}_2\text{O}$), trisodium citrate dihydrate ($\text{C}_8\text{H}_5\text{Na}_3\text{O}_7 \cdot 2\text{H}_2\text{O}$), anhydrous sodium acetate (NaOAc), ethanol, and ethylene glycol (EG) were purchased from Shanghai Chemical Reagents Co. Polyethylene glycol (PEG) ($M_w = 2000$) was obtained from Aladdin Reagent Corp. (Shanghai, China). The MTT [3-(4,5-dimethylthiazol-2-yl)-2,5-diphenyltetrazolium bromide] assay and other biological reagents were purchased from Sigma Company Ltd. Dulbecco's modified Eagle's medium (DMEM), fetal bovine serum (FBS), the penicillin/streptomycin solution, and the trypsin-EDTA solution were purchased from Gibco (Tulsa, OK). All the other chemicals were of analytical grade, and purified water was produced by a Millipore water purification system.

Synthesis of Fe_3O_4 Particles: The citrate-stabilized Fe_3O_4 (Fe_3O_4 -Cit) (240 nm) particles were prepared by a modified solvothermal reaction. Briefly, Iron (III) chloride ($\text{FeCl}_3 \cdot 6\text{H}_2\text{O}$) (1.08 g), trisodium citrate dihydrate ($\text{C}_8\text{H}_5\text{Na}_3\text{O}_7 \cdot 2\text{H}_2\text{O}$) (0.24 g), and anhydrous sodium acetate (NaOAc) (1.20 g) were first dissolved in ethylene glycol (EG) (20 mL) with sonicated an ultrasonic bath for 5 min, and under then vigorous stirring for 30 min. Then the resulting solution was transferred into a Teflon-lined stainless-steel autoclave with a capacity of 50 mL. The autoclave was sealed and heated at 200 °C for 10 h and then cooled to room temperature.

The polyethylene glycol-stabilized Fe_3O_4 (Fe_3O_4 -PEG) (300 nm) particles were synthesized by modified reduction reaction between $\text{FeCl}_3 \cdot 6\text{H}_2\text{O}$ and EG in a solvothermal system. First, $\text{FeCl}_3 \cdot 6\text{H}_2\text{O}$ (1.08 g) was dissolved in 40 mL EG to form an orange solution. Subsequently, NaOAc (3.60 g) was added, followed by vigorously stirring for 30 min. Herein, PEG ($M_w = 2000$) with a dosages of 1.0 g was added into the system. Afterward, the mixture was sealed in a Teflon-lined stainless-steel autoclave and maintained at 200 °C. After a 10 h reaction period, the autoclave was cooled to room temperature. The obtained ferrite particles were washed three times with water and ethanol and collected with the help of a magnet. The final products were dispersed in ethanol for the further use.

Characterization: A field emission scanning electron microscope (FESEM, Ultra 55, Zeiss, Germany) equipped with an energy-dispersive

X-ray spectrum was used to determine the morphology and composition of the Fe_3O_4 -PEG (300 nm) and Fe_3O_4 -Cit (240 nm). Transmission electron microscopy (TEM) images were obtained on a Tecnai G2 20 TWIN transmission electron microscope. Hydrodynamic diameters and zeta potentials were measured by using a dynamic light scattering (DLS) particle size analyzer (Malvern Nano-ZS90) at a scattering angle of 90°. The X-ray diffraction (XRD) measurements were recorded on an X'pert PRO Diffractometer to determine the composition of Fe_3O_4 particles. X-ray photoelectron spectroscopy (XPS) measurements were analyzed by employed an ESCA-Lab-200i-XL spectrometer with monochromatic Al K α radiation (1486.6 eV). Magnetic characterization was carried out with a vibrating sample magnetometer (VSM) on a Model 6000 physical property measurement system (Quantum, USA) at 300 K. UV-vis spectra were performed using a Perkin-Elmer Lambda 750 spectrophotometer. ICP-AES was performed to determine the concentration of the Fe iron contents in the Fe_3O_4 -Cit and Fe_3O_4 -PEG by a P-4010 spectrometer (Hitachi, Japan). T_2 -weighted images of Fe_3O_4 -PEG and Fe_3O_4 -Cit were obtained under a 7 T clinical MRI scanner (BioSpec 70/30 USR, Bruker, Switzerland).

Full Wave Numerical Simulations: We use COMSOL for the full wave numerical simulations, which is based on finite element method (FEM) and multiphysical fields coupling analysis. A background plane wave is traveling to the Fe_3O_4 and Fe_2O_3 particles. Due to the symmetry of the problem, only one-quarter of the sphere is modeled. A region of water around the sphere is also modeled. A perfectly matched layer (PML) domain is outside of the water domain and acts as an absorber of the scattered field. The PML should not be within the reactive near-field of the scatter, placing it a half-wavelength away. At last, we can get the absorption from the volume integration of resistive losses $Q_{rh} = \frac{1}{2} \operatorname{Re}(J^* E^*)$, where J is the local electric current and E is the local electric field.

In Vitro Experiments:

Cell Lines and Culture Conditions: 293T and A549 cells obtained from Chinese Academy of Sciences Cells Bank, Shanghai, China, were routinely cultured in RPMI-1640 cell medium supplemented with 10% FBS, 100 U mL $^{-1}$ penicillin, and 100 mg mL $^{-1}$ streptomycin, at 37 °C in 5% CO $_2$ and 95% air atmosphere with >95% humidity. All experiments were performed on cells in the logarithmic phase of growth.

Cell Viability Assay: The cytotoxicity assay of Fe_3O_4 -Cit (240 nm) and Fe_3O_4 -PEG (300 nm) particles against 293T cells were assessed by the standard MTT assay. The cells were seeded in 96-well plates at a density of 8×10^3 viable cells per well and incubated for 24 h to allow cell attachment. Then the cells were incubated with Fe_3O_4 -PEG and Fe_3O_4 -Cit at indicated concentrations from 5 to 1000 $\mu\text{g mL}^{-1}$, respectively. After 48 h, the medium were replaced with 20 μL of MTT (5 mg mL $^{-1}$), and the cells were incubated for an additional 4 h in dark. Upon the removal of MTT solution, the purple formazan crystals generated by live cells were dissolved with 150 μL DMSO. The relative cell viability was determined by comparing the absorbance at 490 nm or 570 nm (Epoch2, BIO-TEK Instruments Inc., USA) with control wells containing only cell culture medium.

A549 cells were selected for the cell viability experiment. They were seeded in 96-well plates with a density of 10^4 cells per well, and allowed to adhere for 24 h prior to assay. Then, the PBS, Fe_3O_4 -Cit, and Fe_3O_4 -PEG were added to the cells with the same concentration of 100 $\mu\text{g mL}^{-1}$, respectively. The laser was applied to irradiate the cells at a power density of 6.6 W cm^{-2} from 0 to 300 s. After the another incubation time of 24 h, the cells were incubated with 5 mg mL $^{-1}$ MTT for 4 h in dark and then mixed with dimethyl sulfoxide after the supernatant was removed. The OD value at 490 or 570 nm was read using the microplate reader (Epoch2, BIO-TEK Instruments Inc. USA). Cell viability was determined by the percentage of OD value of the study group over the control group.

Confocal Laser Scanning Microscopy: A549 cells grown to 80% in 96-well plate were incubated with Fe_3O_4 -Cit (240 nm) and Fe_3O_4 -PEG (300 nm) at a concentration of 50 $\mu\text{g mL}^{-1}$ for 1 h. Then cells irradiated

by 808 nm laser under a power density of 6.6 W cm^{-2} for 300 s. Then the cell suspension was collected and washed briefly in PBS and then transfer into the confocal laser glass dishes. Before incubation for an additional 0.5 h, the cells were stained with $2.0 \times 10^{-6} \text{ M}$ Calcein-AM and $2.0 \times 10^{-6} \text{ M}$ EthD-1 (Ethidium homodimer-1). Fluorescence images of cells were collected using a C2+ confocal microscope (Nikon, Japan). The excitation/emission wavelength of Calcein-AM is 495/515 nm by argon laser and which EthD-1 was 495/635 nm laser.

Flow Cytometry Analysis: To investigate the photothermal ablation of A549 cells by Fe_3O_4 -Cit (240 nm) and Fe_3O_4 -PEG (300 nm) with the 808 nm laser irradiation using flow cytometry, Fe_3O_4 -Cit and Fe_3O_4 -PEG dispersion was added to a 96-well cell culture plate containing A549 cells with a density of $5-10 \times 10^3$ cells/well in RPMI-1640 medium supplemented with 10% FBS and 1% penicillin-streptomycin (50 and 100 mg mL^{-1} in RPMI-1640 medium solution), then the A549 cells were incubated for 4 h at 37°C in 5% CO_2 and 95% air atmosphere with >95% humidity. Then, a group of cell solution was exposed to an 808 nm laser at a power intensity of 6.6 W cm^{-2} for 300 s. After the laser irradiation treated, the cells were harvested and washed with PBS, and then PI and Annexin-V-FITC were added directly to the cell suspended in the binding buffer ($10 \times 10^{-3} \text{ M}$ HEPES, $140 \times 10^{-3} \text{ M}$ NaCl, $2.5 \times 10^{-3} \text{ M}$ CaCl₂, pH 7.4). The cells were incubated in the dark for 15 min at 37°C . A549 cells were stained with Annexin-V-FITC (FL1) and PI (FL3) and analyzed by Gallios flow cytometry with excitation at 488 nm (Gallios, USA).

Tumor Model: Male BALB/c nude mice (4 weeks old, $\approx 20 \text{ g}$ body weight) were purchased from Shanghai BK Laboratory Animal Co., Ltd., China. Animal care and handing procedures were in agreement with the guidelines evaluated and approved by the ethics committee of Fudan University. A549 subcutaneous tumors were inoculated by subcutaneous injection of 2×10^6 cells suspended in 100 μL PBS into the flank region. The tumor size was monitored every week by a digital caliper. The tumor-bearing mice (with the longest dimension $\approx 5.0 \text{ mm}$) were randomized into three therapy groups ($n = 6$ per group): PBS with laser treated (Group I), Fe_3O_4 -Cit (240 nm) with laser treated (Group II), Fe_3O_4 -PEG (300 nm) with laser treated (Group III), each group of dispersion with a concentration of 0.25 mg mL^{-1} was tail intravenous injected into mice (injection volume of 200 μL). One hour with magnetic targeting after injection, the tumors were exposed to the 808 nm NIR laser at the power density of 6.6 W cm^{-2} for 5 min. The tumor surface temperatures were recorded by an infrared camera thermographic system. The tumor sizes were measured by a caliper every other day. The tumor volume was calculated as the formula (tumor length) \times (tumor width)²/2. At 20th day, all the mice were euthanized, and the tumors were dissected and weighed.

Statistical Analysis: The statistical analysis of the samples was conducted by Student's t-test, p-value <0.05 were considered statistically significant (*) and p < 0.01 were very significant (**). All data reported are means \pm standard deviations, unless otherwise noted.

Supporting Information

Supporting Information is available from the Wiley Online Library or from the author.

Acknowledgements

This work was financially supported by National Natural Science Foundation of China (Grant Nos. 51273047, 51473037, 11474057, and 11174055) and the "Shu Guang" project (12SG07) supported by Shanghai Municipal Education Commission and Shanghai Education Development Foundation.

Received: March 8, 2016

Revised: March 24, 2016

Published online: April 25, 2016

- [1] Y. Yin, A. P. Alivisatos, *Nature* **2005**, *437*, 664.
- [2] a) J. Guo, W. Yang, C. Wang, *Adv. Mater.* **2013**, *25*, 5196; b) D. A. Giljohann, D. S. Seferos, W. L. Daniel, M. D. Massich, P. C. Patel, C. A. Mirkin, *Angew. Chem. Int. Ed.* **2010**, *49*, 3280; c) L. H. Reddy, J. L. Arias, J. Nicolas, P. Couvreur, *Chem. Rev.* **2012**, *112*, 5818; d) J. Tang, B. Kong, H. Wu, M. Xu, Y. C. Wang, Y. L. Wang, D. Y. Zhao, G. F. Zheng, *Adv. Mater.* **2013**, *25*, 6569.
- [3] S. I. Stoeva, F. W. Huo, J. S. Lee, C. A. Mirkin, *J. Am. Chem. Soc.* **2005**, *127*, 15362.
- [4] Y. Deng, D. Qi, C. Deng, X. Zhang, D. Zhao, *J. Am. Chem. Soc.* **2008**, *130*, 28.
- [5] M. Zhao, L. Josephson, Y. Tang, R. Weissleder, *Angew. Chem. Int. Ed.* **2003**, *42*, 1375.
- [6] a) S. J. Son, J. Reichel, B. He, M. Schuchman, S. B. Lee, *J. Am. Chem. Soc.* **2005**, *127*, 7316; b) M. Lewin, N. Carlesso, C. H. Tung, X. W. Tang, D. Cory, D. T. Scadden, R. Weissleder, *Nat. Biotechnol.* **2000**, *18*, 410; c) J. Kim, S. Park, J. E. Lee, S. M. Jin, J. H. Lee, I. S. Lee, I. Yang, J. S. Kim, S. K. Kim, M. H. Cho, T. Hyeon, *Angew. Chem. Int. Ed.* **2006**, *45*, 7754; d) N. L. Rosi, C. A. Mirkin, *Chem. Rev.* **2005**, *105*, 1547; e) X. Song, H. Gong, S. Yin, L. Cheng, C. Wang, Z. Li, Y. Li, X. Wang, G. Liu, Z. Liu, *Adv. Funct. Mater.* **2014**, *24*, 1194; f) C. C. Huang, P. Y. Chang, C. L. Liu, J. P. Xu, S. P. Wu, W. C. Kuo, *Nanoscale* **2015**, *7*, 12689.
- [7] M. Y. Liao, P. S. Lai, H. P. Yu, H. P. Lin, C. C. Huang, *Chem. Commun.* **2012**, *48*, 5319.
- [8] a) H. W. Duan, M. Kuang, X. X. Wang, Y. A. Wang, H. Mao, S. M. Nie, *J. Phys. Chem. C* **2008**, *112*, 8127; b) H. Chen, J. Burnett, F. Zhang, J. Zhang, H. Paholak, D. Sun, *J. Mater. Chem. B* **2014**, *2*, 757.
- [9] J. F. Zeng, L. H. Jing, Y. Hou, M. X. Jiao, R. R. Qiao, Q. J. Jia, C. Y. Liu, F. Fang, H. Lei, M. Y. Gao, *Adv. Mater.* **2014**, *26*, 2694.
- [10] a) D. Ling, N. Lee, T. Hyeon, *Acc. Chem. Res.* **2015**, *48*, 1276; b) Y. Liu, T. Chen, C. C. Wu, L. P. Qiu, R. Hu, J. Li, S. Cansiz, L. Q. Zhang, C. Cui, G. Z. Zhu, M. X. You, T. Zhang, W. H. Tan, *J. Am. Chem. Soc.* **2014**, *136*, 12552.
- [11] X. Zhang, X. Xu, T. Li, M. Lin, X. Lin, H. Zhang, H. Sun, B. Yang, *ACS Appl. Mater. Interfaces* **2014**, *6*, 14552.
- [12] a) X. H. Huang, I. H. El-Sayed, W. Qian, M. A. El-Sayed, *J. Am. Chem. Soc.* **2006**, *128*, 2115; b) L. Cheng, C. Wang, L. Feng, K. Yang, Z. Liu, *Chem. Rev.* **2014**, *114*, 10869; c) E. K. Lim, T. Kim, S. Paik, S. Haam, Y. M. Huh, K. Lee, *Chem. Rev.* **2015**, *115*, 327; d) Z. Zhou, Y. Sun, J. Shen, J. Wei, C. Yu, B. Kong, W. Liu, H. Yang, S. Yang, W. Wang, *Biomaterials* **2014**, *35*, 7470.
- [13] a) X. J. Wang, C. Wang, L. Cheng, S. T. Lee, Z. Liu, *J. Am. Chem. Soc.* **2012**, *134*, 7414; b) H. Y. Liu, T. L. Liu, X. L. Wu, L. L. Li, L. F. Tan, D. Chen, F. Q. Tang, *Adv. Mater.* **2012**, *24*, 755.
- [14] a) K. Yang, S. A. Zhang, G. X. Zhang, X. M. Sun, S. T. Lee, Z. A. Liu, *Nano Lett.* **2010**, *10*, 3318; b) D. Chen, C. Wang, X. Nie, S. Li, R. Li, M. Guan, Z. Liu, C. Chen, C. Wang, C. Shu, L. Wan, *Adv. Funct. Mater.* **2014**, *24*, 6621.
- [15] a) S. Chou, B. Kaehr, J. Kim, B. M. Foley, M. De, P. E. Hopkins, J. Huang, C. J. Brinker, V. P. Dravid, *Angew. Chem. Int. Ed.* **2013**, *52*, 4160; b) L. Cheng, J. Liu, X. Gu, H. Gong, X. Shi, T. Liu, C. Wang, X. Wang, G. Liu, H. Xing, W. Bu, B. Sun, Z. Liu, *Adv. Mater.* **2014**, *26*, 1886; c) M. Zhou, R. Zhang, M. A. Huang, W. Lu, S. L. Song, M. P. Melancon, M. Tian, D. Liang, C. Li, *J. Am. Chem. Soc.* **2010**, *132*, 15351.
- [16] a) Y. Liu, K. Ai, J. Liu, M. Deng, Y. He, L. Lu, *Adv. Mater.* **2013**, *25*, 1353; b) L. Cheng, K. Yang, Q. Chen, Z. Liu, *ACS Nano* **2012**, *6*, 5605; c) C. Wang, H. Xu, C. Liang, Y. Liu, Z. Li, G. Yang, H. Cheng, Y. Li, Z. Liu, *ACS Nano* **2013**, *7*, 6782.
- [17] a) M. Chu, Y. Shao, J. Peng, X. Dai, H. Li, Q. Wu, D. Shi, *Biomaterials* **2013**, *34*, 4078; b) S. Shen, S. Wang, R. Zheng, X. Zhu, X. Jiang, D. Fu, W. Yang, *Biomaterials* **2015**, *39*, 67.

- [18] a) A. Espinosa, R. Di Corato, J. Kolosnjaj-Tabi, P. Flaud, T. Pellegriño, C. Wilhelm, *ACS Nano* **2016**, *10*, 2436; b) X. M. Guo, Z. Wu, W. Li, Z. H. Wang, Q. P. Li, F. F. Kong, H. B. Zhang, X. L. Zhu, Y. P. P. Du, Y. Jin, Y. Z. Du, J. You, *ACS Appl. Mater. Interfaces* **2016**, *8*, 3092.
- [19] a) J. Liu, Z. K. Sun, Y. H. Deng, Y. Zou, C. Y. Li, X. H. Guo, L. Q. Xiong, Y. Gao, F. Y. Li, D. Y. Zhao, *Angew. Chem. Int. Ed.* **2009**, *48*, 5875; b) J. Ge, Y. Hu, M. Biasini, W. P. Beyermann, Y. Yin, *Angew. Chem. Int. Ed.* **2007**, *46*, 4342.
- [20] H. Deng, X. L. Li, Q. Peng, X. Wang, J. P. Chen, Y. D. Li, *Angew. Chem. Int. Ed.* **2005**, *44*, 2782.
- [21] S. Xuan, Y. Wang, J. Yu, K. C. F. Leung, *Chem. Mater.* **2009**, *21*, 5079.
- [22] P. Huang, J. Lin, W. Li, P. Rong, Z. Wang, S. Wang, X. Wang, X. Sun, M. Aronova, G. Niu, R. D. Leapman, Z. Nie, X. Chen, *Angew. Chem. Int. Ed.* **2013**, *52*, 13958.
- [23] Y. Liu, K. Ai, J. Liu, M. Deng, Y. He, L. Lu, *Adv. Mater.* **2013**, *25*, 1353.
- [24] J. Cui, R. Jiang, S. Xu, G. Hu, L. Wang, *Small* **2015**, *11*, 4183.
- [25] a) M. D. Shultz, J. U. Reveles, S. N. Khanna, E. E. Carpenter, *J. Am. Chem. Soc.* **2007**, *129*, 2482; b) M. Y. Liao, C. H. Wu, P. S. Lai, J. Yu, H. P. Lin, T. M. Liu, C. C. Huang, *Adv. Funct. Mater.* **2013**, *23*, 2044.
- [26] R. Bliem, E. McDermott, P. Ferstl, M. Setvin, O. Gamba, J. Pavelec, M. A. Schneider, M. Schmid, U. Diebold, P. Blaha, L. Hammer, G. S. Parkinson, *Science* **2014**, *346*, 1215.
- [27] a) V. Goossens, J. Wielant, S. Van Gils, R. Finsy, H. Terryn, *Surf. Interface Anal.* **2006**, *38*, 489; b) W. F. J. Fontijn, P. J. vanderZaag, M. A. C. Devillers, V. A. M. Brabers, R. Metselaar, *Phys. Rev. B* **1997**, *56*, 5432.
- [28] J. Tang, M. Myers, K. A. Bosnick, L. E. Brus, *J. Phys. Chem. B* **2003**, *107*, 7501.
- [29] T. Yamashita, P. Hayes, *Appl. Surf. Sci.* **2008**, *254*, 2441.
- [30] A. Mekki, D. Holland, C. F. McConville, M. Salim, *J. Non-Cryst. Solids* **1996**, *208*, 267.
- [31] a) L. H. Reddy, J. L. Arias, J. Nicolas, P. Couvreur, *Chem. Rev.* **2012**, *112*, 5818; b) M. Mahmoudi, H. Hofmann, B. Rothen-Rutishauser, A. Petri-Fink, *Chem. Rev.* **2011**, *112*, 2323; c) B. Szalay, E. Tátrai, G. Nyíró, T. Vezér, G. Dura, *J. Appl. Toxicol.* **2012**, *32*, 446.
- [32] M. Perez-Hernandez, P. Del Pino, S. G. Mitchell, M. Moros, G. Stepien, B. Pelaz, W. J. Parak, E. M. Galvez, J. Pardo, J. M. de la Fuente, *ACS Nano* **2015**, *9*, 52.
- [33] Z. Li, S. Yin, L. Cheng, K. Yang, Y. Li, Z. Liu, *Adv. Funct. Mater.* **2014**, *24*, 2312.